

Physics-Informed Deep Contrast Source Inversion: A Unified Framework for Inverse Scattering Problems

Haoran Sun, *Graduate Student Member*, Daoqi Liu, *Graduate Student Member*, Hongyu Zhou, *Graduate Student Member*, Maokun Li, *Fellow, IEEE*, Shenheng Xu, *Member, IEEE*, and Fan Yang, *Fellow, IEEE*

Abstract—Inverse scattering problems are critical in electromagnetic imaging and medical diagnostics but are challenged by their nonlinearity and diverse measurement scenarios. This paper proposes a physics-informed deep contrast source inversion framework (DeepCSI) for fast and accurate medium reconstruction across various measurement conditions. Inspired by contrast source inversion (CSI) and neural operator methods, a residual multilayer perceptron (ResMLP) is employed to model current distributions in the region of interest under different transmitter excitations, effectively linearizing the nonlinear inverse scattering problem and significantly reducing the computational cost of traditional full-waveform inversion. By modeling medium parameters as learnable tensors and utilizing a hybrid loss function that integrates state equation loss, data equation loss, and total variation regularization, DeepCSI establishes a fully differentiable framework for joint optimization of network parameters and medium properties. Compared with conventional methods, DeepCSI offers advantages in terms of simplicity and universal modeling capabilities for diverse measurement scenarios, including phase-less and multi-frequency observation. Simulations and experiments demonstrate that DeepCSI achieves high-precision, robust reconstruction under full-data, phaseless data, and multifrequency conditions, outperforming traditional CSI methods and providing an efficient and universal solution for complex inverse scattering problems.

Index Terms—inverse scattering problems, contrast source inversion, physics-informed deep learning, phaseless data inversion, multi-frequency data inversion.

I. INTRODUCTION

ELECTROMAGNETIC inverse scattering is a technique for reconstructing the physical property distribution of domain of interest (DOI) from measurement data [1]. Due to its ability to accurately invert the position, shape, size, and material properties of unknown objects, it has been widely applied in electromagnetic (EM) imaging [2], [3], medical diagnostics [4], nondestructive testing [5], and geophysical exploration [6]. However, as applications expand, the inherent nonlinearity and ill-posedness of inverse scattering problems (ISPs), combined with the need for adaptability to complex

measurement scenarios, pose significant challenges for existing methods.

Traditional EM inverse scattering methods can be categorized into non-iterative and iterative methods based on their solution processes. Non-iterative methods, such as Born approximation (BA) [7], Rytov approximation (RA) [8], back-projection algorithm (BP) [9], linear sampling method (LSM) [10], decomposition of the time reversal operator method (DORT) [11], etc., achieve efficient inversion by linearizing the ISPs under certain assumptions but are limited to qualitative imaging with insufficient accuracy [12]. In contrast, iterative methods formulate the ISP as an optimization problem and achieve quantitative imaging by minimizing the objective function [1]. These methods include Gauss-Newton-type methods [13], [14], Born iterative method (BIM) [15], distorted Born iterative method (DBIM) [16], contrast source inversion (CSI) [17], and subspace-based optimization method (SOM) [18], [19]. Typically, iterative methods incorporate regularization terms, such as Tikhonov regularization [20], total variation regularization [21], and multiplicative regularization [22], to introduce prior information, constrain the solution space, and mitigate the ill-posedness of ISPs, ensuring stable convergence. Although iterative methods achieve higher reconstruction accuracy, they are computationally expensive, sensitive to initial guesses, and prone to local optima, which limits their applicability in complex scenarios.

In recent years, the rapid development of artificial intelligence has demonstrated significant potential for improving computational efficiency and numerical accuracy in EM modeling [23]–[25], inverse problems [26]–[28], antenna design, and optimization [29]–[31], leading to the emergence of numerous data-driven inverse scattering methods. These methods are categorized into purely data-driven and physics-data hybrid methods. In 2019, Li et al. introduced DeepNIS [32], which employs deep neural networks to map non-iterative inversion results to ground truth, achieving high accuracy in specific cases similar to training data while significantly enhancing inversion speed. Wei et al. explored the impact of various non-iterative methods on reconstruction accuracy, proposing a better inversion scheme [33]. Due to their simplicity and computational efficiency, these methods have been applied to phaseless data inversion [34] and underground detection [35], exhibiting promising performance. However, their direct reliance on neural network output results in poor interpretability and unclear generalization boundaries, limiting the reliability

This work was supported in part by the National Natural Science Foundation of China under Grant 62401035 and Grant 61971263; in part by the Beijing Science and Technology Plan under Grant No.Z231100004623007; in part by the Institute for Precision Medicine, Tsinghua University; and in part by the BGP Inc.

Haoran Sun, Daoqi Liu, Hongyu Zhou, Maokun Li, Shenheng Xu and Fan Yang are with Department of Electronic Engineering, Beijing National Research Center for Information Science and Technology (BNRist), Tsinghua University, Beijing 100084, China. (e-mail: maokunli@tsinghua.edu.cn).

in practical applications. To address these issues, physics-data hybrid inverse scattering methods have been developed. Guo et al. proposed an update-learning-based scheme [36], replacing the model update calculation in conjugate gradient method (CG) with neural network, achieving comparable accuracy to traditional methods using only four cascaded modules. Similarly, Shan et al. introduced the neural Born iteration method [37], utilizing two convolutional subnetworks to simulate the alternating updates of contrast and total field in BIM. Liu et al. proposed SOM-Net [38], employing cascaded U-nets to mimic the iterative process of traditional SOM. These hybrid methods integrate physical models with deep learning to ensure physically consistent outputs, improving inversion efficiency and reliability. Nevertheless, as supervised learning approaches, they require extensive offline training to ensure accuracy and exhibit limited generalization, struggling to adapt to diverse measurement scenarios.

To address the limitations of existing inverse scattering methods, such as sensitivity to initial values, limited generalization, reliance on large training datasets, and challenges in adapting to diverse measurement scenarios, this paper proposes DeepCSI, a physics-informed deep contrast source inversion framework inspired by CSI [39] and neural operator methods [40]. DeepCSI is an unsupervised case-by-case inversion method, where the training process is the inversion process. In this framework, a lightweight residual multilayer perceptron (ResMLP) is employed to predict current distributions under different transmitters, using concatenated and position-encoded mesh and source coordinates as inputs and outputting current values at each mesh node. Meanwhile, medium parameters are modeled as learnable tensors. A hybrid loss function, incorporating state equation loss, data equation loss, and total variation regularization, is constructed to guide the joint optimization of network parameters and medium properties. Leveraging automatic differentiation, DeepCSI forms a fully differentiable framework for accurate inversion. Compared to existing unsupervised iterative methods, DeepCSI offers simpler implementation and higher inversion accuracy while flexibly adapting to diverse measurement scenarios, including phase-less and multi-frequency data. Finally, the proposed method is validated through multiple simulation cases and Fresnel experimental data, and compared with traditional CSI and MRCSI methods. Simulation and experimental results demonstrate that DeepCSI achieves superior inversion accuracy, lower sensitivity to initial guesses, and robust performance under diverse noise conditions. Most importantly, DeepCSI effectively utilizes measurement data across full-data, phase-less, and multifrequency scenarios, showcasing its effectiveness and application potential.

This article is organized as follows. Section II briefly reviews inverse scattering problems. Section III formulates traditional CSI and MRCSI method. The DeepCSI method, including ResMLP-based induced currents prediction and medium property inversion scheme for both full and phaseless data, is proposed in Section IV. The simulation and experimental data inversion results are given to validate the proposed method in Sections V. Discussions and conclusions are presented in Sections VI and VII, respectively.

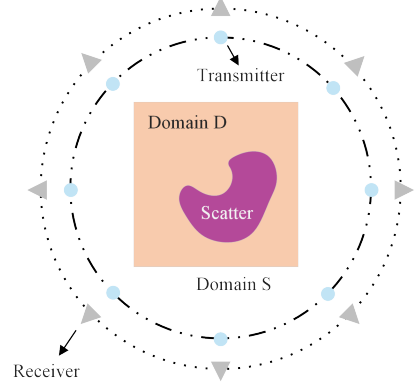


Fig. 1. Typical setup of 2-D inverse scattering problems.

II. INVERSE SCATTERING PROBLEMS

Consider a two-dimensional DOI in free space, where an arbitrarily shaped unknown scatterer is illuminated by TM-polarized line sources arranged in a circular configuration. The total field is measured by receivers placed around the DOI, as illustrated in Fig. 1. Under this setup, the relationship among the incident field E^{inc} , the scattered field E^{sca} , and the total field E^{tot} can be expressed as [41]:

$$E^{tot}(r) = E^{inc}(r) + k_b^2 \int_D G_D(r, r') \chi(r') E^{tot}(r') dr', r \in D \quad (1)$$

$$E^{sca}(r) = k_b^2 \int_D G_s(r, r') \chi(r') E^{tot}(r') dr', r \in S \quad (2)$$

where, $k_b = \sqrt{\omega\mu_0\epsilon_0}$ denotes the wavenumber in free space, $\chi = \epsilon_r/\epsilon_0 - 1$ represents the scatterer contrast, and ϵ_r is the relative permittivity of the scattering object. G_D and G_S denote the Green's functions inside and outside the scatterer, respectively, while D and S correspond to the DOI and the observation domain. By discretizing the DOI and applying pulse basis functions along with a point-matching strategy, the continuous integral equation can be transformed into a linear system of equations, which can be expressed as:

$$E^{tot} = E^{inc} + G_D \chi E^{tot} \quad (3)$$

$$E^{sca} = G_s \chi E^{tot} \quad (4)$$

Therefore, the ISP essentially aims to obtain the scatterer contrast χ from the measured scattered field \mathbf{d}^* . This is typically formulated as an optimization problem, with the cost function defined as follows:

$$\mathcal{L}(\chi) = \|\mathbf{d}^* - S(\chi)\|^2 + L_{TV}(\chi) \quad (5)$$

where $S(\cdot)$ represents the forward modeling function, and $L_{TV}(\cdot)$ represents the total variation regularization term. As indicated by the above formulations, the ISP is inherently highly nonlinear and ill-posed, which remains the fundamental challenge that has hindered its effective solution.

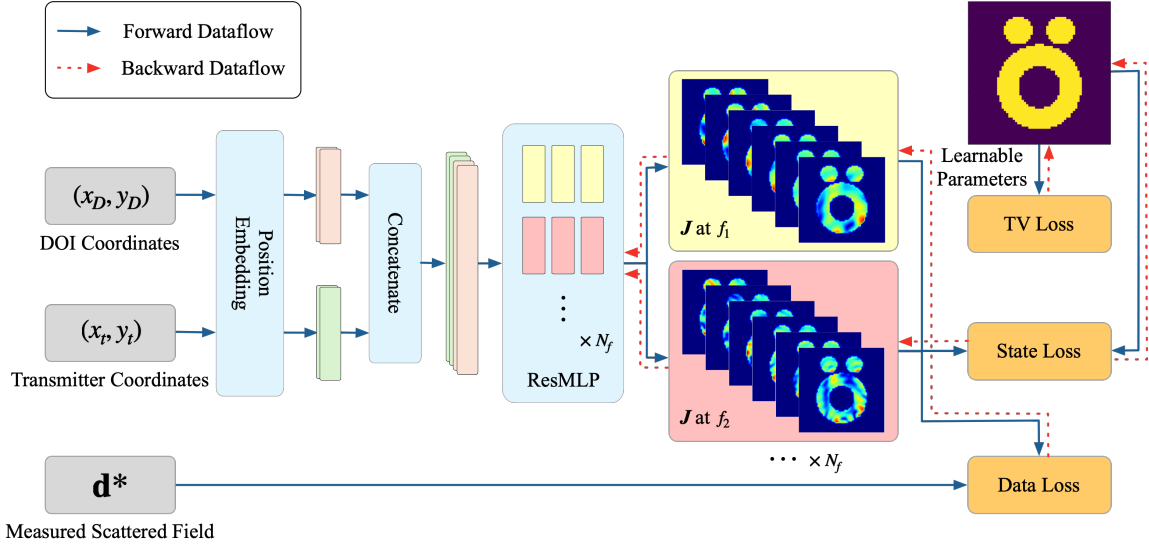


Fig. 2. The framework of DeepCSI. Each subnet in the ResMLP module predicts the induced current distribution at a specific frequency. The subnets share the same architecture but have independent weights.

III. CONTRAST SOURCE INVERSION METHOD

Unlike the method described in Section II, which directly formulates ISP as an optimization problem, the CSI method introduces a contrast source ω , also known as induced current J [39]. This reformulates the original problem as two linear optimization subproblems, with the cost functions expressed as:

$$\begin{aligned} \mathcal{L}_{CSI}(\omega, \chi) &= \mathcal{L}_D(\omega, \chi) + \mathcal{L}_S(\omega) \\ &= \frac{\|\omega - \chi E^{inc} - \chi G_D \omega\|_2^2}{\|\chi E^{inc}\|_2^2} + \frac{\|E^{sca} - G_S \omega\|_2^2}{\|E^{sca}\|_2^2} \end{aligned} \quad (6)$$

Additionally, multiplicative regularization term has been introduced to enhance inversion accuracy. In 2001, Van Den Berg et al. incorporated a weighted L_2 TV constraint, achieving state of the art in CSI [17]. The regularization term is expressed as:

$$\mathcal{F}_{TV}(\chi) = \frac{\sum_{i=1}^{N^2} \left(\|\nabla \chi_i\|^2 + \delta^2(\chi') \right)^{\frac{p}{2}}}{\sum_{i=1}^{N^2} \left(\|\nabla \chi'_i\|^2 + \delta^2(\chi') \right)^{\frac{p}{2}}} \quad (7)$$

$$\delta^2(\chi') = \mathcal{L}_D(\omega, \chi') \cdot \Delta^2 \quad (8)$$

where p denotes the norm of TV regularization, which is set to 2 in this paper. Δ represents the mesh size of the discrete domain D . χ and χ' denote the contrast at the current and previous iterations, respectively. The cost function incorporating the multiplicative regularization can be expressed as:

$$\mathcal{L}_{MRCI}(\omega, \chi) = \mathcal{L}_{CSI}(\omega, \chi) \mathcal{F}_{TV}(\chi) \quad (9)$$

In solving this optimization problem, CSI minimizes the cost function by alternately updating the contrast source ω and the contrast χ . At the n -th iteration, the update expression for the contrast source is given by:

$$\omega_n = \omega_{n-1} + \alpha_n^\omega v_n \quad (10)$$

where v_n is the Polak–Ribière conjugate gradient direction, which can be computed by evaluating the gradient of the cost function with respect to the contrast source. The step size α_n^ω for updating the contrast source is obtained via a line search method. The detailed formulations of α_n^ω and v_n can be found in [42]. After updating the contrast source, the total field can be updated as:

$$E_n^{tot} = E^{inc} + G_D \omega_n \quad (11)$$

Subsequently, the contrast can be updated as:

$$\chi_n = \chi_{n-1} + \alpha_n^\chi d_n \quad (12)$$

where the update direction d_n is also the Polak–Ribière conjugate gradient direction, which requires computing the gradient of the cost function with respect to the contrast for the update. The step size α_n^χ for contrast update is similarly determined via a line search method. Detailed formulas can be found in [42]. This indicates that the traditional CSI optimization process is complex and requires adjusting gradient-based update rules for different measurements, which poses significant implementation challenges.

IV. PHYSICS-INFORMED DEEP CONTRAST SOURCE INVERSION FRAMEWORK

Current mainstream EM inverse scattering methods are primarily gradient-based, requiring manual derivation of the gradient calculation formulas. Additionally, the update rules vary under different measurement conditions or regularization settings, which results in limited adaptability to diverse scenarios. To address this issue, inspired by CSI and neural operator methods, the DeepCSI framework is proposed, as illustrated in Fig. 2. In this framework, a ResMLP is used as a global basis function to model induced currents, facilitating the mapping between spatial coordinates and current distributions. Simultaneously, the target dielectric parameters are set as learnable tensors, and a hybrid loss function is introduced to

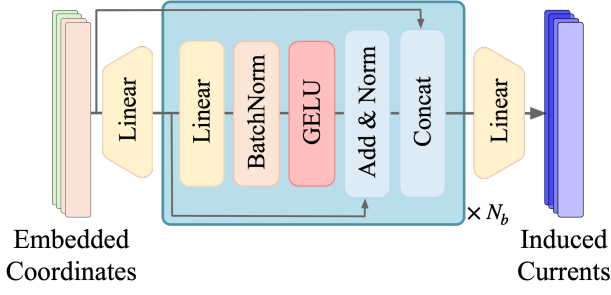


Fig. 3. The architecture of the ResMLP in DeepCSI.

jointly optimize the ResMLP parameters and medium property. This enables DeepCSI to accurately and efficiently invert the property distribution case by case without the need for training. Furthermore, by simply modifying the loss function, the framework can adapt to various application scenarios, including phaseless and multi-frequency measurements.

A. ResMLP-based Induced Currents Prediction

In DeepCSI framework, the ResMLP module is used to predict the induced current distribution in DOI, with the detailed workflow shown in Fig. 2. As illustrated in the figure, the inputs to the ResMLP module include spatial coordinates within the DOI and transmitter coordinate information, while the output is the predicted induced current for different frequencies and transmitters. To address the spectral bias inherent in MLPs [43], we first apply frequency-domain positional encoding to the spatial coordinates. The encoded coordinate expression is given by [44]:

$$\gamma(x, y) = \begin{bmatrix} \cos(2x), \sin(2x), \dots, \cos(2^M x), \sin(2^M x) \\ \cos(2y), \sin(2y), \dots, \cos(2^M y), \sin(2^M y) \end{bmatrix}^T \quad (13)$$

where M is a hyperparameter that controls the spectral bandwidth of the input coordinate vector. After positional encoding, the spatial coordinates and transmitter coordinates are concatenated and used as the input to the ResMLP module, enabling accurate fitting of the high-frequency induced current distribution.

The architecture of each ResMLP subnet used in this paper is shown in Fig. 3. Each subnet consists of N_b stacked modules, with each module comprising a linear layer with a hidden dimension of 256, batch normalization, a GELU activation function, and residual connections. Given the differences in induced current distributions at various frequencies, multiple ResMLP subnets with the same architecture but independent weights are used to predict the current distribution at each frequency, ensuring the accuracy of the induced current predictions. The predicted induced currents consist of two channels, representing the real and imaginary parts. After reshaping and combining the channels, the resulting complex-valued induced current distribution is shown in Fig. 2.

B. Medium Property Inversion Scheme

After obtaining the induced current distribution in the DOI from the ResMLP module, by substituting $J = \chi E^{tot}$, the

equations can be further rewritten as:

$$J = \chi E^{inc} + \chi G_D J \quad (14)$$

$$E^{sca} = G_S J \quad (15)$$

where, Eq.(14) is typically referred to as the state equation, while Eq.(15) is the data equation [17]. Thus, the ISP is reformulated as an optimization problem for the contrast χ and induced current J under the constraints of the state and data equations. This transformation process is consistent with traditional CSI methods. The key difference in this paper is that the contrast is directly modeled as a learnable tensor, enabling simultaneous optimization and updating of both the contrast and ResMLP network parameters via PyTorch's automatic differentiation and the Adam optimizer [45]. Therefore, this method eliminates the need for manual derivation of gradient formulas and update rules required by traditional CSI methods.

Furthermore, the inversion loss function used in DeepCSI is similar to that of CSI. When the measurement data includes both amplitude and phase, also known as full data, the expression of loss function is:

$$\begin{aligned} \mathcal{L}^{fd} &= \mathcal{L}_S^{fd} + \mathcal{L}_D^{fd} + \alpha \mathcal{L}_{TV}^{fd} \\ &= \frac{\|J - \chi E^{inc} - \chi G_D J\|_2}{\|\chi E^{inc}\|_2} + \frac{\|\mathbf{d}^* - G_S J\|_2}{\|\mathbf{d}^*\|_2} + \alpha \sum |\nabla \chi| \end{aligned} \quad (16)$$

where \mathbf{d}^* represents the measured scattered field data, and α is a hyperparameter controlling the weight of the regularization term. In this paper, its initial value is set to 0.1, which linearly decays to 0.05 during the inversion process.

In practical EM sensing, when the transmitter frequency is high, accurate phase measurement is often difficult to achieve. Therefore, it is crucial to study EM inverse scattering based on phaseless data (PD-ISP). Existing PD-ISP research typically builds upon traditional full data inverse scattering methods (FD-ISP), which require the derivation of new gradient update rules and significant modifications to inversion code [46]. This increases the complexity of research and application in PD-ISP and makes it challenging to directly apply the latest FD-ISP techniques to PD-ISP. In contrast, the proposed DeepCSI method enables the implementation of PD-ISP by modifying just a single line of loss function code. The corresponding expression for the loss function is:

$$\begin{aligned} \mathcal{L}^{pd} &= \mathcal{L}_S^{pd} + \mathcal{L}_D^{pd} + \alpha \mathcal{L}_{TV}^{pd} \\ &= \frac{\|J - \chi E^{inc} - \chi G_D J\|_2}{\|\chi E^{inc}\|_2} \\ &\quad + \frac{\|\mathbf{d}^* - |E_r^{inc} + G_S J|\|_2}{\|\mathbf{d}^*\|_2} + \beta \sum |\nabla \chi| \end{aligned} \quad (17)$$

where E_r^{inc} denotes the incident field directly radiated from the transmitter to the receiver, and \mathbf{d}^* represents the measured phaseless total field data. The parameter β is a hyperparameter controlling the weight of the regularization term, set consistently with α . The main reason for using total field here is that under phaseless measurement conditions, only phaseless total field data can be obtained, unlike full-data measurements where the scattered field can be derived by subtracting the incident field.

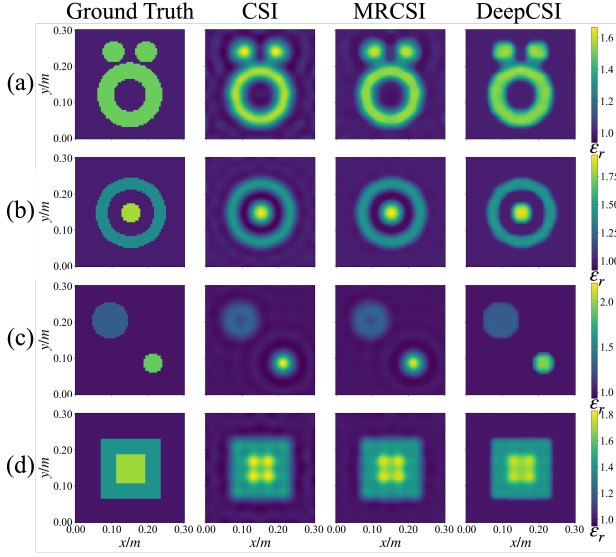


Fig. 4. Comparison of FD inversion results for CSI, MRCSI, and DeepCSI methods at 3 GHz. The first column represents the ground truth, while columns 2 to 4 represent the inversion results of CSI, MRCSI, and DeepCSI methods, respectively. (a)~(d) display four representative test cases.

V. NUMERICAL RESULTS

In this section, the performance of the proposed DeepCSI method is validated through inversion of synthetic and experimental data, and compare the results with those obtained using the traditional CSI [39] and MRCSI [17] methods. In the DeepCSI method, two Adam optimizers are used to separately optimize the ResMLP parameters and the medium properties, with initial learning rates of 0.05 and 0.1, respectively. Both optimizers employ an exponential decay learning rate schedule with a decay factor of 0.1 and a decay period of 2000.

To quantitatively assess the accuracy of the inversion results from different methods, relative root mean square error (RMSE) and structural similarity index (SSIM) are introduced. The respective formulas are given as follows:

$$\text{RMSE} = \frac{\|p_{\text{inv}} - p_{\text{truth}}\|_2}{\|p_{\text{truth}}\|_2} = \sqrt{\frac{\sum (p_{\text{inv}} - p_{\text{truth}})^2}{\sum (p_{\text{truth}})^2}} \quad (18)$$

$$\text{SSIM} = \frac{(2\mu_{\text{inv}}\mu_{\text{truth}} + C_1)(2\sigma_{\text{inv},\text{truth}} + C_2)}{(\mu_{\text{inv}}^2 + \mu_{\text{truth}}^2 + C_1)(\sigma_{\text{inv}}^2 + \sigma_{\text{truth}}^2 + C_2)} \quad (19)$$

where p_{inv} and p_{truth} represent the inversion results and the ground truth, respectively. μ_{inv} and μ_{truth} denote the mean values of p_{inv} and p_{truth} , while σ_{inv} and σ_{truth} represent the corresponding variances. $\sigma_{\text{inv},\text{truth}}$ indicates the covariance between the inversion result and the ground truth. $C_1 = (K_1L)^2$ and $C_2 = (K_2L)^2$ are two small constants introduced to avoid division by zero. Among them, K_1 and K_2 are two hyperparameters, set to 0.01 and 0.03, respectively. L represents the dynamic range of pixel values in the results, which is set to 1 in this paper.

The proposed DeepCSI method, as well as the benchmark methods such as CSI and MRCSI [17], are implemented using the PyTorch framework [47] and run on a single Nvidia RTX 4090 GPU.

TABLE I
PERFORMANCE COMPARISON OF THE FD INVERSION RESULTS OF THE CSI, MRCSI, AND DEEPCSI METHODS ON FOUR DIFFERENT TEST CASES

| Case No. | Method | RMSE↓ | SSIM↑ |
|----------|---------|---------------|---------------|
| (a) | CSI | 0.0778 | 0.6531 |
| | MRCSI | 0.0754 | 0.7285 |
| | DeepCSI | 0.0597 | 0.8573 |
| (b) | CSI | 0.0665 | 0.7993 |
| | MRCSI | 0.0637 | 0.8598 |
| | DeepCSI | 0.0532 | 0.9112 |
| (c) | CSI | 0.0644 | 0.7770 |
| | MRCSI | 0.0631 | 0.8239 |
| | DeepCSI | 0.0410 | 0.9610 |
| (d) | CSI | 0.0493 | 0.7406 |
| | MRCSI | 0.0467 | 0.8102 |
| | DeepCSI | 0.0331 | 0.9098 |

A. Synthetic Data Inversion

In the synthetic data inversion, the size of the DOI is $0.3 \times 0.3 \text{ m}^2$, with 16 transmit antennas and 32 receive antennas uniformly distributed on circles with radii of 2 m and 2.2 m, respectively. In the single-frequency inversion of this section, the transmit wave frequency is 3 GHz, while in the multi-frequency inversion, the frequencies are 3, 4, and 5 GHz. The scattering field data used for inversion are obtained through Method of Moments (MoM) [48]. To avoid the inverse crime, all cases in this section divide the DOI into 128×128 grids in the forward modeling process, while during inversion, the DOI is divided into 64×64 grids. Furthermore, to thoroughly evaluate the performance of the algorithm, 5% Gaussian white noise is added to the scattering field data. The scattering field with added noise can be expressed as:

$$\hat{E}_{\text{sca}} = E_{\text{sca}} + \sigma_n * \mu_{\text{sca}} * \mathcal{N}(0, 1) \quad (20)$$

where $\mathcal{N}(0, 1)$ denotes a Gaussian distribution with a mean of 0 and a variance of 1, μ_{sca} represents the mean energy of the received scattered field, and σ_n denotes the added white noise level.

1) *Full Data Inversion*: In this section, the proposed algorithm is first applied to perform full-data (FD) inversion on several cases at a frequency of 3 GHz, and the results are compared with traditional CSI and MRCSI methods. The final inversion results and performance metrics are shown in Fig.4 and Table I. As seen in the figure, for the four different cases, the inversion results obtained using the proposed DeepCSI method not only yield a contrast and shape closer to the true values, but also exhibit fewer artifacts in the background region, with particularly noticeable improvements in Case (c). The data in Table I further demonstrate that, in all four cases, the proposed method achieves lower RMSE and higher SSIM, with a particularly significant advantage in the SSIM metric. These results indicate that the proposed method offers a substantial improvement in inversion accuracy compared to traditional CSI and MRCSI methods.

To further demonstrate the performance of the DeepCSI method in FD-ISP, the inversion update process for the four cases is shown in Fig. 5. From the figure, it can be seen that the DeepCSI method, starting from a uniform background, requires only 200 iterations of Adam optimization to obtain an initial result, and after 500 iterations, the result closely matches

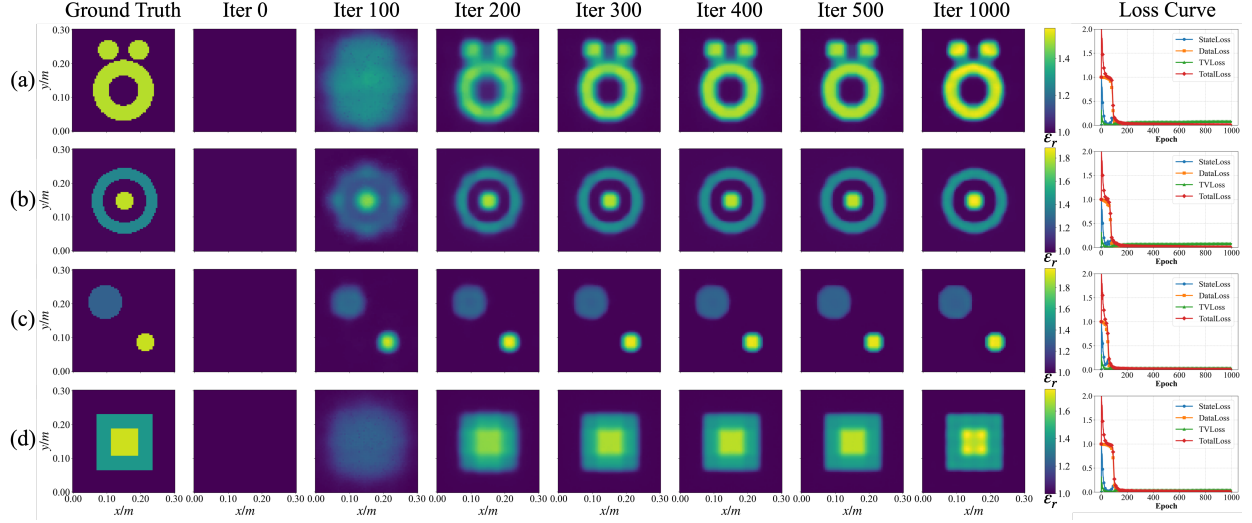


Fig. 5. The update process and loss curve of the DeepCSI method for FD inversion at 3 GHz. The first column represents the ground truth, while columns 2 to 8, labeled with "Iter n", present the inversion results after the n-th iteration. The final column displays the loss curve of the DeepCSI method for the corresponding test case. (a)~(d) present four representative test cases.

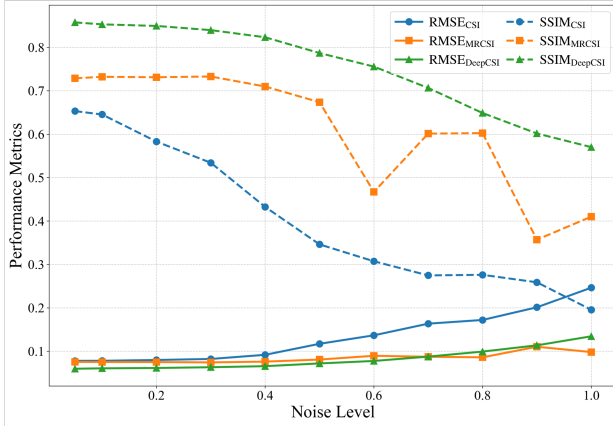


Fig. 6. The RMSE and SSIM curves of FD inversion results obtained using CSI, MRCSI, and DeepCSI methods under varying noise levels.

the ground truth. Considering that each Adam optimization update takes approximately 0.05 seconds on a GPU platform, the proposed algorithm achieves satisfactory inversion results in just 10 to 25 seconds. In contrast, under the same hardware conditions, traditional CSI and MRCSI methods require about 100 iterations to converge, taking approximately 80 seconds. Thus, it is evident that the proposed method not only offers higher inversion accuracy but also significantly improves optimization efficiency compared to traditional inversion methods.

In practical measurements, noise interference in the data is inevitable, and therefore, inversion algorithms are usually required to have good noise resistance. To evaluate the performance of the proposed DeepCSI method under various noise conditions, 11 different levels of Gaussian white noise, including 5%, 10% to 100%, are added to the scattering field data. The noisy scattering field data are then inverted using the proposed method. The RMSE and SSIM curves of the inversion results obtained by CSI, MRCSI and DeepCSI methods under varying noise levels are illustrated in Fig.

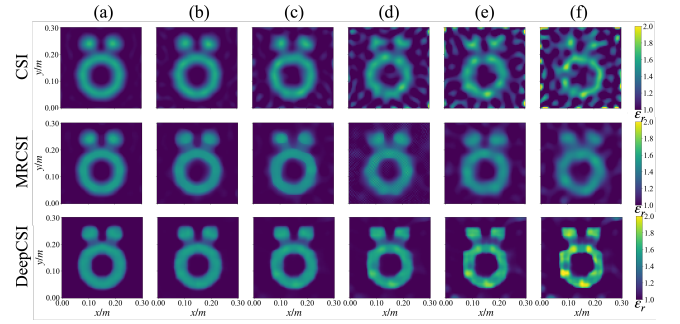


Fig. 7. Inversion results for the Austria model using the CSI, MRCSI, and DeepCSI methods under different noise levels. (a)~(f) represent the inversion results at noise levels of 5%, 20%, 40%, 60%, 80%, and 100%, respectively.

6. As shown in the figure, as the noise level increases, the inversion accuracy of all three methods gradually decreases. However, regardless of the noise level, the proposed method consistently outperforms the CSI method and slightly exceeds the MRCSI method, particularly in terms of the SSIM metric. This indicates that the proposed method has better noise resistance compared to traditional inversion methods.

To further illustrate the inversion accuracy of the proposed method at different noise levels, taking the Austria model as an example, the inversion results of the DeepCSI and the CSI-based methods are visualized as shown in Fig. 7. As shown in the figure, when the noise level exceeds 40%, the results from traditional inversion algorithms begin to exhibit noticeable artifacts, and the target boundaries gradually become blurred as the noise level increases. In contrast, the inversion results obtained using the proposed method maintain a clean background, with the target boundary remaining clear. Although there are some deviations in the inverted medium parameters, the overall inversion accuracy still outperforms the traditional CSI and MRCSI methods, demonstrating strong noise resistance. It is worth noting that although the noise

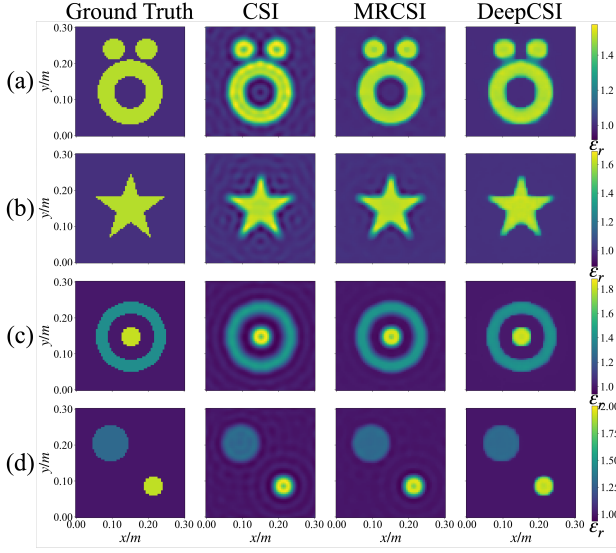


Fig. 8. Comparison of MF inversion results for CSI, MRCSI, and DeepCSI methods at 3,4,5 GHz. The first column represents the ground truth, while columns 2 to 4 represent the inversion results of CSI, MRCSI, and DeepCSI methods, respectively. (a)~(d) display four representative test cases.

TABLE II

PERFORMANCE COMPARISON OF THE MF INVERSION RESULTS OF THE CSI, MRCSI, AND DEEPCSI METHODS ON FOUR DIFFERENT TEST CASES

| Case No. | Method | RMSE↓ | SSIM↑ |
|----------|---------|----------------|---------------|
| (a) | CSI | 0.0586 | 0.7885 |
| | MRCSI | 0.0550 | 0.8734 |
| | DeepCSI | 0.0452 | 0.9235 |
| (b) | CSI | 0.0570 | 0.8046 |
| | MRCSI | 0.0543 | 0.8979 |
| | DeepCSI | 0.04290 | 0.9471 |
| (c) | CSI | 0.0599 | 0.7965 |
| | MRCSI | 0.0559 | 0.8759 |
| | DeepCSI | 0.0357 | 0.9627 |
| (d) | CSI | 0.0477 | 0.8373 |
| | MRCSI | 0.0453 | 0.9168 |
| | DeepCSI | 0.0285 | 0.9829 |

level is 100%, the scattering field data are not completely overwhelmed by the noise, as indicated in Eq. 20. Instead, some scattering field information with amplitudes higher than the average is retained, enabling the proposed method to achieve quantitative inversion of the target without the need for a noise reduction module.

2) *Multi-Frequency Data Inversion*: In the ISP problem, multi-frequency (MF) measurements are often used to improve inversion accuracy by incorporating more target information, which requires the inversion method to be flexible and compatible with MF measurement data. To evaluate the performance of the proposed DeepCSI method under MF measurements, scattering field data at 3, 4, and 5 GHz are used to invert targets with various shapes, including the Austria and Star models. The inversion results obtained from the proposed method, as well as those from the traditional CSI and MRCSI methods, are shown in Fig. 8, and the corresponding performance metrics are presented in Table II.

As shown in Table II, compared to the single-frequency (SF) inversion results in Table I, the RMSE of the inversion results from all three methods decreases and the SSIM improves

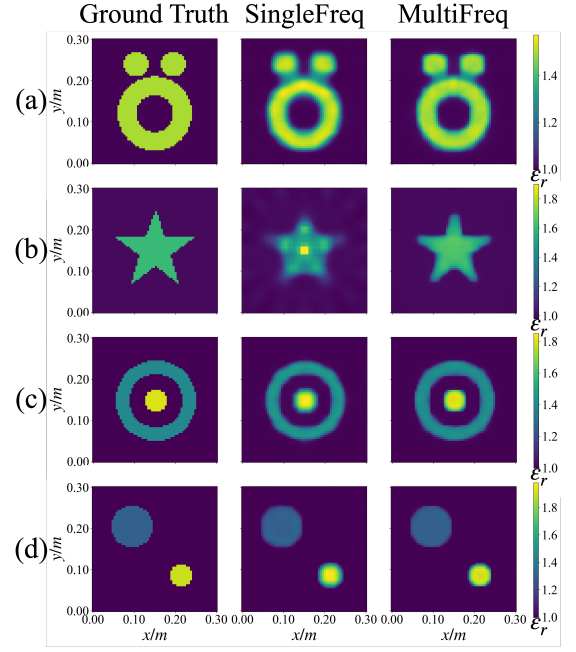


Fig. 9. Comparison of PD inversion results of the DeepCSI method under SF and MF measurements. The first column represents the ground truth, while columns 2 to 3 represent the inversion results of DeepCSI method under SF and MF measurements, respectively. (a)~(d) display four representative test cases.

TABLE III

PERFORMANCE COMPARISON OF THE PD INVERSION RESULTS OF THE DEEPCSI METHOD UNDER SF AND MF MEASUREMENTS ON FOUR DIFFERENT TEST CASES

| Case No. | Method | RMSE↓ | SSIM↑ |
|----------|------------|---------------|---------------|
| (a) | SF-DeepCSI | 0.0613 | 0.8497 |
| | MF-DeepCSI | 0.0490 | 0.9090 |
| (b) | SF-DeepCSI | 0.3153 | 0.7847 |
| | MF-DeepCSI | 0.0443 | 0.9425 |
| (c) | SF-DeepCSI | 0.0557 | 0.9058 |
| | MF-DeepCSI | 0.0373 | 0.9571 |
| (d) | SF-DeepCSI | 0.0417 | 0.9599 |
| | MF-DeepCSI | 0.0301 | 0.9802 |

under MF measurements. However, the proposed DeepCSI method still achieves higher accuracy in MF inversion compared to the traditional CSI and MRCSI methods. Furthermore, as seen in Fig. 8, the DeepCSI method obtains more accurate target shapes, with a permittivity distribution closer to the ground truth and fewer artifacts in the background, especially in Cases (a) and (c), where the radial thickness of the rings is more consistent with the true values. Therefore, it can be concluded that the DeepCSI method effectively utilizes MF data to further enhance inversion accuracy, demonstrating superior performance over traditional CSI and MRCSI methods in MF measurement scenarios.

3) *Phaseless Data Inversion*: To validate the effectiveness of the DeepCSI method for phaseless data (PD) inversion, this section evaluates the PD inversion performance of the proposed method using multiple models, including Austria and Star. Given that MF data are often used in phaseless measurements to ensure inversion accuracy, this section applies the DeepCSI method to invert both SF scattered field data

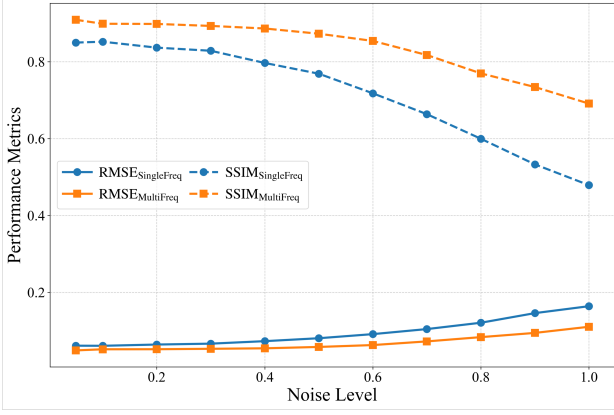


Fig. 10. The RMSE and SSIM curves of PD inversion results obtained using DeepCSI methods under SF and MF measurements at different noise levels.

at 3 GHz and MF scattered field data at 3, 4, and 5 GHz. The resulting inversion results are shown in Fig. 9, and the corresponding inversion accuracy is quantified and presented in Table III.

As shown in Fig. 9, the proposed method can achieve the target inversion using phaseless measurement under SF. In most cases, the reconstructed target shape, size, and permittivity are highly accurate. Only in the case (b), the inversion result of DeepCSI show some deviation from the ground truth, though they still adequately reflect the shape and permittivity of the target. Furthermore, when PD at MF is used, the inversion results from the proposed method show more accurate medium parameters and clearer edges, particularly achieving accurate inversion of the target shape in case (b). This demonstrates that the DeepCSI method can achieve accurate inversion of targets without phase information and the introduction of MF measurement data can further enhance the accuracy of phaseless inversion. Meanwhile, it can be seen from Table III that the performance metrics of the proposed method under SF and MF phaseless measurements are very close to those obtained under FD measurements, indicating that the DeepCSI method can effectively leverages phaseless measurement data and achieve accurate target inversion by combining EM physics and the Adam optimization strategy.

Furthermore, to evaluate the noise robustness of the proposed DeepCSI method under phaseless inversion conditions, Gaussian white noise at 11 different levels, ranging from 5% to 100%, is added to the total field data. The inversion of noisy phaseless total field data using the proposed method under both SF and MF conditions is performed, and the resulting RMSE and SSIM metrics as functions of noise levels are presented in Fig. 10. As shown in the figure, with the increase in noise levels, the accuracy of the inversion results decreases in both cases. However, even with 100% Gaussian white noise added, the RMSE of the SF inversion results from the proposed method remains below 0.2, with an SSIM close to 0.5, indicating that the inversion results still basically reflect the target information. Additionally, it can be observed that the RMSE and SSIM of the MF measurement inversion results are consistently better than those of the SF

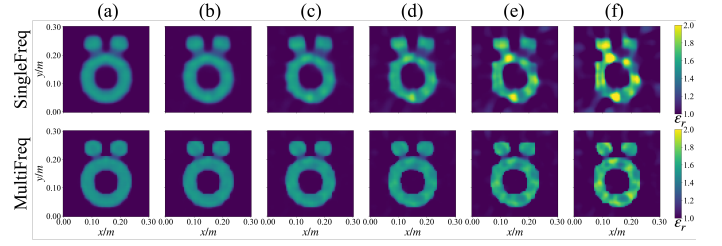


Fig. 11. PD inversion results for the Austria model using DeepCSI method under SF and MF measurements at different noise levels. (a)~(f) represent the inversion results at noise levels of 5%, 20%, 40%, 60%, 80%, and 100%, respectively.

measurements, highlighting the advantages and necessity of MF data in phaseless measurements.

To further illustrate the impact of noise on DeepCSI phaseless inversion, the inversion results for the Austria target under SF and MF measurements at different noise levels are visualized in Fig. 11. As shown in the figure, as the noise level increases, the target shape in the SF inversion results gradually deviates from the ground truth, and the accuracy of the permittivity inversion decreases. However, even with 100% noise added, the SF reconstruction results from the proposed method still exhibit a clear contour and approximate shape of the target, indicating that the method retains good noise resistance even under SF measurement conditions. Furthermore, it can be observed that, regardless of the noise level, the target shape, size, and permittivity in MF inversion results are closer to the ground truth. This demonstrates that the proposed DeepCSI method can effectively utilize MF phaseless measurement data and achieve accurate target inversion even in the presence of significant noise.

B. Experimental Data Inversion

In this section, Fresnel experimental data are used to further validate the proposed DeepCSI method [49]. Three sets of experimental data, including FoamDielExtTM, FoamDielIntTM, and FoamTwinDielTM, are inverted. During the Fresnel data collection, the FoamDielIntTM and FoamDielExtTM cases are illuminated by eight line sources uniformly distributed on a circle with a radius of 1.67 m, while the FoamTwinDielTM case is illuminated by 18 line sources, similarly distributed. For each illumination, scattered field data are collected by 241 receivers distributed along the same circumference. The frequency range of the line sources used in the Fresnel data collection is from 2 GHz to 10 GHz.

In this experiment, the DOI size is set to $0.17 \times 0.17 \text{ m}^2$. Scattered field data at 3 GHz are first used for inversion validation, and the DeepCSI method inversion results, along with comparisons to traditional CSI and MRCSI methods, are shown in Fig. 12. As shown in the figure, compared to traditional methods, the proposed DeepCSI method achieves higher inversion accuracy. Especially for the small cylinders with high contrast, the DeepCSI method can more accurately reconstruct their edge positions and medium parameters. Furthermore, the scattered field data corresponding to the inversion results for each case are computed and compared with the measured

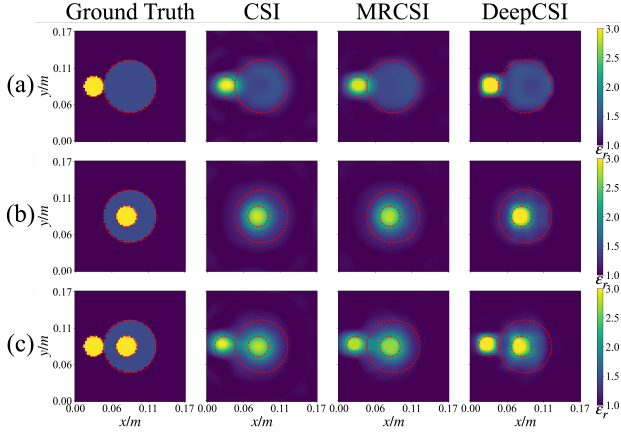


Fig. 12. Comparison of FD inversion results for CSI, MRCSI, and DeepCSI methods on Fresnel experimental data at 3 GHz. The first column represents the ground truth, while columns 2 to 4 represent the inversion results of CSI, MRCSI, and DeepCSI methods. (a)~(c) represents FoamDielExTM, FoamDielIntTM, and FoamTwinDielTM, respectively. The red dashed line indicates the position and size of the real target.

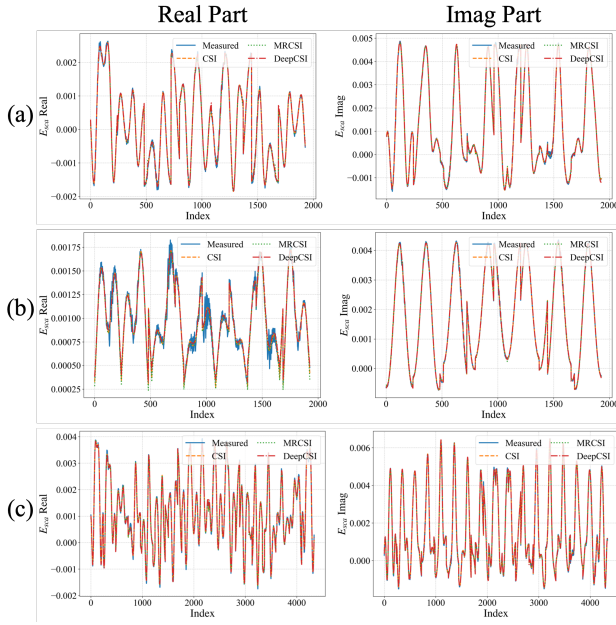


Fig. 13. Comparison of measured and inverted scattered field data using CSI, MRCSI, and DeepCSI methods on Fresnel experimental data at 3 GHz. The first and second columns represent the real and imaginary parts of the scattered field data, respectively. (a)~(c) represents three different test cases, namely FoamDielExTM, FoamDielIntTM and FoamTwinDielTM. The measured and inverted scattered field data are marked with different line styles in the figure.

scattered field data, as shown in Fig. 13. From the figure, it is evident that the inversion results align well with the measured data, further demonstrating that the DeepCSI method can effectively fit the scattered data, highlighting its effectiveness in SF inversion.

To more accurately quantify the inversion accuracy of the proposed method, the RMSE and SSIM of the inversion results from the three methods are presented in Table IV. As shown in the table, the RMSE and SSIM of the proposed method outperform those of the CSI and MRCSI methods. Even in case (a), the SSIM of the proposed method exceeds 0.84,

TABLE IV
PERFORMANCE COMPARISON OF THE FD INVERSION RESULTS FOR CSI, MRCSI, AND DEEPCSI METHODS ON FRESNEL EXPERIMENTAL DATA AT 3 GHz

| Case No. | Method | RMSE↓ | SSIM↑ |
|----------|---------|---------------|---------------|
| (a) | CSI | 0.1874 | 0.5985 |
| | MRCSI | 0.1870 | 0.7364 |
| | DeepCSI | 0.1359 | 0.8435 |
| (b) | CSI | 0.1314 | 0.5511 |
| | MRCSI | 0.1302 | 0.6756 |
| | DeepCSI | 0.1078 | 0.8204 |
| (c) | CSI | 0.1973 | 0.5498 |
| | MRCSI | 0.1997 | 0.6937 |
| | DeepCSI | 0.1730 | 0.7770 |

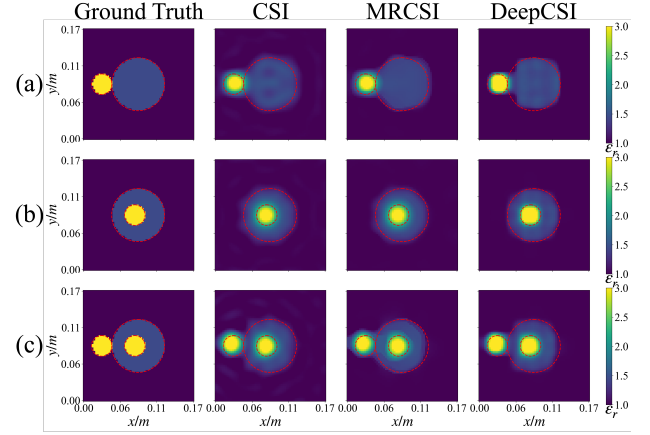


Fig. 14. Comparison of MF inversion results for CSI, MRCSI, and DeepCSI methods on Fresnel experimental data at 3, 4, 5 GHz. The first column represents the ground truth, while columns 2 to 4 represent the inversion results of CSI, MRCSI, and DeepCSI methods. (a)~(c) represents FoamDielExTM, FoamDielIntTM, and FoamTwinDielTM, respectively. The red dashed line indicates the position and size of the real target.

reflecting a high inversion accuracy. However, in case (c), all three methods show slightly lower inversion accuracy. This is primarily due to the lower quality of the scattered field data collected at 3 GHz for this case, which resulted in less accurate inversion of the large cylinder with lower contrast, thereby affecting the overall inversion accuracy.

To further improve inversion quality, Fresnel scattered field data at 3, 4, and 5 GHz are used for inversion. The results of DeepCSI method and its comparison with the traditional CSI and MRCSI methods are shown in Fig. 14, and the corresponding performance metrics are presented in Table V. From this table, it can be seen that the inversion accuracy of all three methods improves under MF conditions, with the DeepCSI method still outperforming the CSI and MRCSI methods. As shown in Fig. 14, the inversion results using the DeepCSI method exhibit clear target contours and accurate medium parameters, demonstrating high inversion accuracy across the three different cases. Specifically, in case (b) and (c), the inversion results of the high contrast small cylinder obtained by DeepCSI show more accurate sizes, positions, and permittivity, which are highly consistent with the ground truth. This further validates the effectiveness of DeepCSI method in MF data inversion.

TABLE V
PERFORMANCE COMPARISON OF THE MF INVERSION RESULTS FOR CSI,
MRCSI, AND DEEPCSI METHODS ON FRESNEL EXPERIMENTAL DATA AT
3,4,5 GHz

| Case No. | Method | RMSE↓ | SSIM↑ |
|----------|---------|---------------|---------------|
| (a) | CSI | 0.1889 | 0.6232 |
| | MRCSI | 0.1867 | 0.8049 |
| | DeepCSI | 0.1161 | 0.8668 |
| (b) | CSI | 0.1162 | 0.7106 |
| | MRCSI | 0.1158 | 0.8140 |
| | DeepCSI | 0.0920 | 0.8923 |
| (c) | CSI | 0.1768 | 0.5867 |
| | MRCSI | 0.1766 | 0.7674 |
| | DeepCSI | 0.1584 | 0.8230 |

VI. DISCUSSION

Inspired by traditional CSI method, the proposed DeepCSI method introduces induced current as an intermediate variable to decompose the ISP into two linear problems, thereby reducing its computational complexity. However, unlike conventional CSI method, DeepCSI uses a deep neural network as the global basis function to represent the induced current, enabling direct prediction of their spatial distribution. Furthermore, by leveraging the Adam optimizer, DeepCSI ensures that the predicted induced current distribution and target property parameters simultaneously satisfy the constraints of both the data and state equations, achieving accurate inversion under FD and PD conditions. A key innovation of DeepCSI lies in its differentiable inverse-scattering solving framework, which integrates an induced current prediction module. By combining PyTorch’s automatic differentiation with Adam optimizer, DeepCSI method achieves end-to-end robust optimization, circumventing the need for manual gradient derivation and update rules, which is a computationally intensive step in traditional methods. This design allows DeepCSI to adapt flexibly to challenging inversion scenarios, such as PD or MF measurements, through simple loss function adjustments.

However, the introduction of the induced current prediction module also presents new challenges. As the frequency of the incident wave increases, the model needs stronger representation ability to fit high-frequency information. Due to the inherent spectral bias of the ResMLP architecture used in this study, deeper network structures and more optimization steps are required to achieve convergence. This leads to a significant increase in computational resources and time, posing a considerable challenge for the application of DeepCSI method in large-scale inverse scattering problems.

VII. CONCLUSION

In this paper, a physics-informed deep contrast source inversion framework is proposed to solve 2-D inverse scattering problems under various measurement conditions. Inspired by CSI and neural operator methods, the DeepCSI method uses ResMLP to predict the induced current distribution in DOI. Meanwhile, the dielectric property is directly set as a learnable tensor. Then, a hybrid loss function, including state equation loss, data equation loss, and total variation regularization, is employed to jointly optimize the ResMLP network parameters and dielectric property, ultimately achieving fast and accurate

inversion of the targets. The numerical experimental results demonstrate that DeepCSI can accurately invert dielectric targets under full-data, phaseless data, and multi-frequency measurement conditions, achieving higher inversion accuracy and efficiency compared to traditional inverse scattering methods. This mainly benefits from the simultaneous optimization of the ResMLP network parameters and dielectric property, as well as the powerful Adam optimizer.

Furthermore, the differentiable nature of the DeepCSI framework enables seamless adaptation to diverse measurement configurations simply by modifying the loss function, significantly reducing the complexity for electromagnetic inverse scattering research and applications. This framework demonstrates native compatibility with the latest inverse scattering techniques, such as VAE-based model compression method [50]. In summary, as a flexible and extendable inverse scattering framework, DeepCSI has great potential for applications. However, due to the inherent spectral bias in the ResMLP architecture, DeepCSI currently faces challenges in solving large-scale inverse scattering problems beyond 10 wavelengths. Future work could explore the use of more advanced network architectures, such as wavelet neural operator, or more complex optimization methods, such as frequency-domain adaptive optimizer, to address this issue and further expand the applicability of the DeepCSI method.

REFERENCES

- [1] X. Chen, *Computational methods for electromagnetic inverse scattering*. John Wiley & Sons, 2018.
- [2] A. Abubakar, P. Van den Berg, and S. Y. Semenov, “Two-and three-dimensional algorithms for microwave imaging and inverse scattering,” *Journal of Electromagnetic Waves and Applications*, vol. 17, no. 2, pp. 209–231, 2003.
- [3] K. Xu, Z. Qian, Y. Zhong, J. Su, H. Gao, and W. Li, “Learning-assisted inversion for solving nonlinear inverse scattering problem,” *IEEE Transactions on Microwave Theory and Techniques*, vol. 71, no. 6, pp. 2384–2395, 2022.
- [4] M. T. Bevacqua, S. Di Meo, L. Crocco, T. Isernia, and M. Pasian, “Millimeter-waves breast cancer imaging via inverse scattering techniques,” *IEEE Journal of Electromagnetics, RF and Microwaves in Medicine and Biology*, vol. 5, no. 3, pp. 246–253, 2021.
- [5] X. Yang, H. Sun, C. Guo, Y. Li, J. Gong, X. Qu, and T. Lan, “Layered media parameter inversion method based on deconvolution autoencoder and self-attention mechanism using gpr data,” *IEEE Transactions on Geoscience and Remote Sensing*, vol. 62, pp. 1–14, 2024.
- [6] A. Abubakar, T. Habashy, V. Druskin, L. Knizhnerman, and D. Alumbaugh, “2.5 d forward and inverse modeling for interpreting low-frequency electromagnetic measurements,” *Geophysics*, vol. 73, no. 4, pp. F165–F177, 2008.
- [7] A. Devaney, “Inversion formula for inverse scattering within the born approximation,” *Optics Letters*, vol. 7, no. 3, pp. 111–112, 1982.
- [8] —, “Inverse-scattering theory within the rytov approximation,” *Optics Letters*, vol. 6, no. 8, pp. 374–376, 1981.
- [9] A. J. Devaney, “A filtered backpropagation algorithm for diffraction tomography,” *Ultrasonic Imaging*, vol. 4, no. 4, pp. 336–350, 1982.
- [10] D. Colton, H. Haddar, and M. Piana, “The linear sampling method in inverse electromagnetic scattering theory,” *Inverse Problems*, vol. 19, no. 6, p. S105, 2003.
- [11] C. Prada, S. Manneville, D. Spoliansky, and M. Fink, “Decomposition of the time reversal operator: Detection and selective focusing on two scatterers,” *The Journal of the Acoustical Society of America*, vol. 99, no. 4, pp. 2067–2076, 1996.
- [12] D. Tajik, R. Kazemivala, and N. K. Nikolova, “Real-time imaging with simultaneous use of born and rytov approximations in quantitative microwave holography,” *IEEE Transactions on Microwave Theory and Techniques*, vol. 70, no. 3, pp. 1896–1909, 2021.

- [13] T. Hohage, "Logarithmic convergence rates of the iteratively regularized gauss-newton method for an inverse potential and an inverse scattering problem," *Inverse Problems*, vol. 13, no. 5, p. 1279, 1997.
- [14] P. Mojabi and J. LoVetri, "Overview and classification of some regularization techniques for the gauss-newton inversion method applied to inverse scattering problems," *IEEE Transactions on Antennas and Propagation*, vol. 57, no. 9, pp. 2658–2665, 2009.
- [15] T. J. Cui, W. C. Chew, A. A. Aydinler, and S. Chen, "Inverse scattering of two-dimensional dielectric objects buried in a lossy earth using the distorted born iterative method," *IEEE Transactions on Geoscience and Remote Sensing*, vol. 39, no. 2, pp. 339–346, 2001.
- [16] W. C. Chew and Y.-M. Wang, "Reconstruction of two-dimensional permittivity distribution using the distorted born iterative method," *IEEE transactions on medical imaging*, vol. 9, no. 2, pp. 218–225, 1990.
- [17] P. M. Van den Berg and A. Abubakar, "Contrast source inversion method: State of art," *Progress in Electromagnetics Research*, vol. 34, no. 11, pp. 189–218, 2001.
- [18] X. Chen, "Subspace-based optimization method for solving inverse-scattering problems," *IEEE Transactions on Geoscience and Remote Sensing*, vol. 48, no. 1, pp. 42–49, 2009.
- [19] G. Oliveri, Y. Zhong, X. Chen, and A. Massa, "Multiresolution subspace-based optimization method for inverse scattering problems," *Journal of the Optical Society of America A*, vol. 28, no. 10, pp. 2057–2069, 2011.
- [20] G. H. Golub, P. C. Hansen, and D. P. O'Leary, "Tikhonov regularization and total least squares," *SIAM Journal on Matrix Analysis and Applications*, vol. 21, no. 1, pp. 185–194, 1999.
- [21] P. Van den Berg and R. E. Kleinman, "A total variation enhanced modified gradient algorithm for profile reconstruction," *Inverse Problems*, vol. 11, no. 3, p. L5, 1995.
- [22] T. Regińska, "A regularization parameter in discrete ill-posed problems," *SIAM Journal on Scientific Computing*, vol. 17, no. 3, pp. 740–749, 1996.
- [23] L. Guo, M. Li, S. Xu, F. Yang, and L. Liu, "Electromagnetic modeling using an fdtd-equivalent recurrent convolution neural network: Accurate computing on a deep learning framework," *IEEE Antennas and Propagation Magazine*, vol. 65, no. 1, pp. 93–102, 2021.
- [24] R. Guo, T. Shan, X. Song, M. Li, F. Yang, S. Xu, and A. Abubakar, "Physics embedded deep neural network for solving volume integral equation: 2-d case," *IEEE Transactions on Antennas and Propagation*, vol. 70, no. 8, pp. 6135–6147, 2021.
- [25] Z. Ma, K. Xu, R. Song, C.-F. Wang, and X. Chen, "Learning-based fast electromagnetic scattering solver through generative adversarial network," *IEEE Transactions on Antennas and Propagation*, vol. 69, no. 4, pp. 2194–2208, 2020.
- [26] Q. Dai, Y. H. Lee, H.-H. Sun, G. Ow, M. L. M. Yusof, and A. C. Yucel, "3dinvnet: A deep learning-based 3d ground-penetrating radar data inversion," *IEEE Transactions on Geoscience and Remote Sensing*, vol. 61, pp. 1–16, 2023.
- [27] T. Shan, Z. Lin, X. Song, M. Li, F. Yang, and S. Xu, "Physics-informed supervised residual learning for 2-d inverse scattering problems," *IEEE Transactions on Antennas and Propagation*, vol. 71, no. 4, pp. 3746–3751, 2023.
- [28] Y. Zhang, M. Lambert, A. Fraysse, and D. Lesselier, "Unrolled convolutional neural network for full-wave inverse scattering," *IEEE Transactions on Antennas and Propagation*, vol. 71, no. 1, pp. 947–956, 2022.
- [29] P. Liu, L. Chen, and Z. N. Chen, "Prior-knowledge-guided deep-learning-enabled synthesis for broadband and large phase shift range metacells in metalens antenna," *IEEE Transactions on Antennas and Propagation*, vol. 70, no. 7, pp. 5024–5034, 2022.
- [30] P. Liu and Z. N. Chen, "Full-range amplitude-phase metacells for sidelobe suppression of metalens antenna using prior-knowledge-guided deep-learning-enabled synthesis," *IEEE Transactions on Antennas and Propagation*, vol. 71, no. 6, pp. 5036–5045, 2023.
- [31] Z. N. Chen, X. Qing, Y. Su, and R. Xu, "Toward metantennas: Metamaterial-based antennas for wireless communications," *IEEE Communications Magazine*, vol. 61, no. 11, pp. 160–165, 2023.
- [32] L. Li, L. G. Wang, F. L. Teixeira, C. Liu, A. Nehorai, and T. J. Cui, "Deepnis: Deep neural network for nonlinear electromagnetic inverse scattering," *IEEE Transactions on Antennas and Propagation*, vol. 67, no. 3, pp. 1819–1825, 2018.
- [33] Z. Wei and X. Chen, "Deep-learning schemes for full-wave nonlinear inverse scattering problems," *IEEE Transactions on Geoscience and Remote Sensing*, vol. 57, no. 4, pp. 1849–1860, 2018.
- [34] K. Xu, L. Wu, X. Ye, and X. Chen, "Deep learning-based inversion methods for solving inverse scattering problems with phaseless data," *IEEE Transactions on Antennas and Propagation*, vol. 68, no. 11, pp. 7457–7470, 2020.
- [35] H. Sun, X. Yang, J. Gong, X. Qu, and T. Lan, "Joint physics and data driven full-waveform inversion for underground dielectric targets imaging," *IEEE Transactions on Geoscience and Remote Sensing*, vol. 60, pp. 1–11, 2022.
- [36] R. Guo, Z. Lin, T. Shan, X. Song, M. Li, F. Yang, S. Xu, and A. Abubakar, "Physics embedded deep neural network for solving full-wave inverse scattering problems," *IEEE Transactions on Antennas and Propagation*, vol. 70, no. 8, pp. 6148–6159, 2021.
- [37] T. Shan, Z. Lin, X. Song, M. Li, F. Yang, and S. Xu, "Neural born iterative method for solving inverse scattering problems: 2d cases," *IEEE Transactions on Antennas and Propagation*, vol. 71, no. 1, pp. 818–829, 2022.
- [38] Y. Liu, H. Zhao, R. Song, X. Chen, C. Li, and X. Chen, "Som-net: Unrolling the subspace-based optimization for solving full-wave inverse scattering problems," *IEEE Transactions on Geoscience and Remote Sensing*, vol. 60, pp. 1–15, 2022.
- [39] P. M. Van Den Berg and R. E. Kleinman, "A contrast source inversion method," *Inverse Problems*, vol. 13, no. 6, p. 1607, 1997.
- [40] N. Kovachki, Z. Li, B. Liu, K. Azizzadenesheli, K. Bhattacharya, A. Stuart, and A. Anandkumar, "Neural operator: Learning maps between function spaces with applications to pdes," *Journal of Machine Learning Research*, vol. 24, no. 89, pp. 1–97, 2023.
- [41] J.-M. Jin, *Theory and computation of electromagnetic fields*. John Wiley & Sons, 2015.
- [42] P. M. van den Berg, A. Abubakar, and J. T. Fokkema, "Multiplicative regularization for contrast profile inversion," *Radio Science*, vol. 38, no. 2, pp. 23–1, 2003.
- [43] N. Rahaman, A. Baratin, D. Arpit, F. Draxler, M. Lin, F. Hamprecht, Y. Bengio, and A. Courville, "On the spectral bias of neural networks," in *International Conference on Machine Learning*. PMLR, 2019, pp. 5301–5310.
- [44] B. Mildenhall, P. P. Srinivasan, M. Tancik, J. T. Barron, R. Ramamoorthi, and R. Ng, "Nerf: Representing scenes as neural radiance fields for view synthesis," *Communications of the ACM*, vol. 65, no. 1, pp. 99–106, 2021.
- [45] D. P. Kingma, "Adam: A method for stochastic optimization," *arXiv preprint arXiv:1412.6980*, 2014.
- [46] L. Li, H. Zheng, and F. Li, "Two-dimensional contrast source inversion method with phaseless data: Tm case," *IEEE Transactions on Geoscience and Remote Sensing*, vol. 47, no. 6, pp. 1719–1736, 2008.
- [47] A. Paszke, "Pytorch: An imperative style, high-performance deep learning library," *arXiv preprint arXiv:1912.01703*, 2019.
- [48] R. F. Harrington, *Field computation by moment methods*. Wiley-IEEE Press, 1993.
- [49] J.-M. Geffrin, P. Sabouroux, and C. Eyraud, "Free space experimental scattering database continuation: Experimental set-up and measurement precision," *Inverse Problems*, vol. 21, no. 6, p. S117, 2005.
- [50] R. Guo, Z. Lin, M. Li, F. Yang, S. Xu, and A. Abubakar, "A non-linear model compression scheme based on variational autoencoder for microwave data inversion," *IEEE Transactions on Antennas and Propagation*, vol. 70, no. 11, pp. 11 059–11 069, 2022.